Bioactive Materials 23 (2023) 247–260

Contents lists available at ScienceDirect

Bioactive Materials

journal homepage: www.keaipublishing.com/en/journals/bioactive-materials

Delivery of coenzyme Q10 loaded micelle targets mitochondrial ROS and enhances efficiency of mesenchymal stem cell therapy in intervertebral disc degeneration

Junyuan Sun [a,1], Fei Yang [b,1], Lianlei Wang [a,1], Haichao Yu [c,d,1], Zhijie Yang [e], Jingjing Wei [e], Krasimir Vasilev [f,g], Xuesong Zhang [d,***], Xinyu Liu [a,**], Yunpeng Zhao [a,*]

[a] Department of Orthopaedics, Qilu Hospital, Cheeloo College of Medicine, Shandong University, Jinan, Shandong, 250012, PR China
[b] School of Pharmaceutical Sciences, Shandong University, Jinan, Shandong, 250012, PR China
[c] School of Medicine, Nankai University, Tianjin, 300071, PR China
[d] Department of Orthopaedics, The Fourth Medical Centre, Chinese People's Liberation Army General Hospital, Beijing, 100048, PR China
[e] Key Laboratory of Colloid and Interface Chemistry, Ministry of Education, School of Chemistry and Chemical Engineering, Shandong University, Jinan, Shandong, 250100, PR China
[f] Academic Unit of STEM, University of South Australia, Mawson Lakes, Adelaide, 5095, South Australia, Australia
[g] College of Medicine and Public Health, Flinders University, Bedford Park, 5042, South Australia, Australia

ARTICLE INFO

Keywords:
Intervertebral disc degeneration
Coenzyme Q10
Mesenchymal stem cell
Reactive oxygen species
Micelle

ABSTRACT

Stem cell transplantation has been proved a promising therapeutic instrument in intervertebral disc degeneration (IVDD). However, the elevation of oxidative stress in the degenerated region impairs the efficiency of mesenchymal stem cells (BMSCs) transplantation treatment via exaggeration of mitochondrial ROS and promotion of BMSCs apoptosis. Herein, we applied an emulsion-confined assembly method to encapsulate Coenzyme Q10 (Co-Q10), a promising hydrophobic antioxidant which targets mitochondria ROS, into the lecithin micelles, which renders the insoluble Co-Q10 dispersible in water as stable colloids. These micelles are injectable, which displayed efficient ability to facilitate Co-Q10 to get into BMSCs *in vitro*, and exhibited prolonged release of Co-Q10 in intervertebral disc tissue of animal models. Compared to mere use of Co-Q10, the Co-Q10 loaded micelle possessed better bioactivities, which elevated the viability, restored mitochondrial structure as well as function, and enhanced production of ECM components in rat BMSCs. Moreover, it is demonstrated that the injection of this micelle with BMSCs retained disc height and alleviated IVDD in a rat needle puncture model. Therefore, these Co-Q10 loaded micelles play a protective role in cell survival and differentiation through antagonizing mitochondrial ROS, and might be a potential therapeutic agent for IVDD.

1. Introduction

Intervertebral disc degeneration (IVDD) is the predominant cause of lower back pain, which can create high medical expenses [1,2]. The nucleus pulposus (NP), annulus fibrosus, and endplate are the basic components in intervertebral disc (IVD) [3]. Among all the components, the NP is a gelatinous, fiber reinforced, isotropic and water-rich core, which constructs the main structure of IVD. It contributes to resistance against compression, and provides a center for rotation movement [4,5]. Various pathological factors, including genetics, aging, trauma or other exogenous stimuli result in IVDD [6]. Meanwhile, IVDD is featured by several structural and histological changes as well as an altered expression of extracellular matrix (ECM) and inflammatory markers [7].

To date, supplementation of exogenous stem cells has displayed therapeutic functions on IVDD in both basic research and preclinical studies [6,8,9]. First, the NP tissue is recognized as an immune

Peer review under responsibility of KeAi Communications Co., Ltd.
* Corresponding author.
** Corresponding author.
*** Corresponding author.
E-mail addresses: zhangxuesong301@163.com (X. Zhang), newyuliu@163.com (X. Liu), lwwzyp@email.sdu.edu.cn (Y. Zhao).
[1] These authors contribute equally.

https://doi.org/10.1016/j.bioactmat.2022.10.019
Received 21 August 2022; Received in revised form 15 October 2022; Accepted 17 October 2022

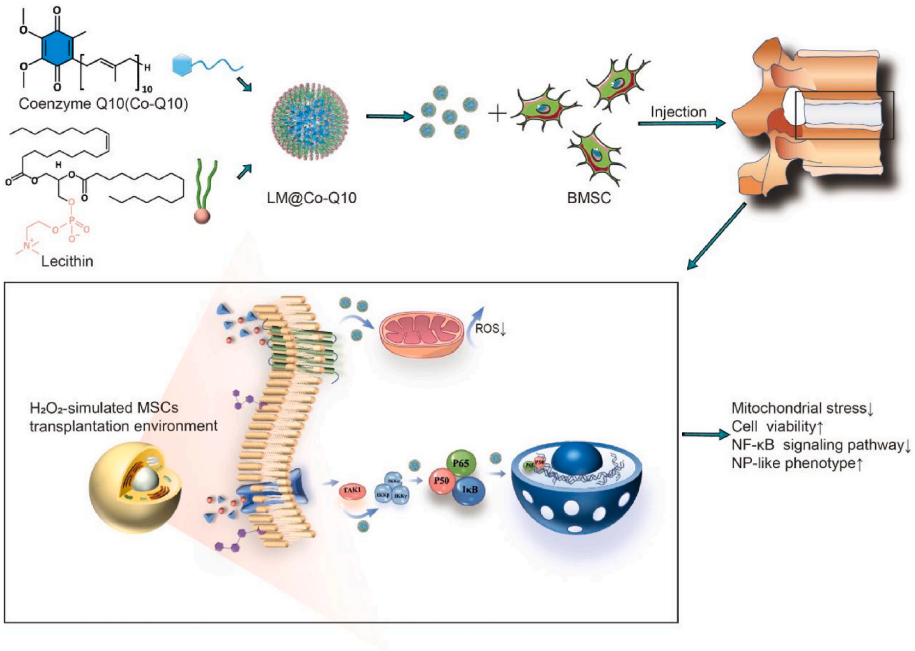

Scheme 1. General schematic of synthesis of injectable Co-Q10-loaded micelle(LM@Co-Q10) as stem cell therapy for intervertebral disc degeneration.

privileged region. This feature of NP area limits immune responses to exogenous stem cell transplantation [10]. Transplantation of several types of stem cells can improve the number of functional cells and ECM, thus maintaining normal functions IVD [11,12]. Therefore, exogenous stem cell transplantation is a potential treatment target for IVDD repair [9]. However, the survival rate of transplanted stem cells and efficiency of cell differentiation in IVD are tough challenges. After stem cell transplantation, a large part of injected cells rapidly become undetectable, implying that the viability as well as functionality of these cells might be markedly damaged [6,8,13]. One predominant explanation for this is the harsh microenvironment at the lesion site, which is mainly caused by excessive reactive oxygen species (ROS) and nonspecific inflammation [14]. Enhanced ROS level in the degenerated NP area reduces the efficiency of IVDD treatment through inhibiting proliferation and increasing apoptosis of stem cells. Oxidative stress also leads to protein carbonylation, hyper-peroxidation and DNA damage to the transplanted stem cells [15,16]. Therefore, it is necessary to figure out the instruments to diminish ROS levels in the degenerated disc microenvironment, which can facilitate the viability and functionality of transplanted cells.

Coenzyme Q10 (Co-Q10) or ubiquinone (2,3-dimethoxy-5-methyl-6-polyprenyl-1,4-benzoquinone) is a lipophilic molecule, which plays a critical role in various conditions. To date, Co-Q10 is detected in the phospholipid bilayer of cellular membranes and is concentrated in the mitochondrial inner membrane. Co-Q10 is identified as a key antioxidant molecule, which is closely associated with cell function and cell viability. Recently, it was reported that Co-Q10 plays a pivotal role in regulation of ferroptosis. Mechanically, Co-Q10 is a mitochondrial electron transport chain component which can make mitochondrial mass, improve mitochondrial function, and inhibit ROS generation [17–19]. It has been revealed that Co-Q10 supplementation can attenuate DNA double strand damage and improve the life cycle of peripheral blood monocytes [20–22]. Moreover, Co-Q10 could suppress cell aging [23–25] and protect several stem cells against hypoxia, oxidative stress and other harsh environments by enhancing survival signals [26,27]. However, coenzyme Q10, as a lipid-soluble molecule, is only soluble in DMSO, which imposes limitations on its use and drug release, therefore, a more suitable drug delivery system is essential.

In this study, we applied an emulsion-template based method to render the hydrophobic Co-Q10 dispersible in water as stable micelles. After the preparation, these Co-Q10 molecules were coated with a layer of phospholipid molecules (lecithin), termed as Co-Q10@lipid micelles (LM@Co-Q10). These micelles were delivered locally into IVDD model together with mesenchymal stem cells (BMSCs), which protects rat BMSCs from oxidative stress and promotes BMSCs to differentiate into an NP-like phenotype (see Scheme 1).

2. Materials and methods

2.1. Materials

All chemicals were used as received without any further purification: chloroform (Adamas, 99.8%), ethanol (≥99%), coenzyme Q10 (Co-Q10, Bidepharm, 97%), lecithin (Adamas, 99%), uranyl acetate (Acmec, 99%). H_2O_2 was purchased from Sigma-Aldrich, USA. The fluorescent probes DiI, DiO and DAPI were purchased from Beyotime (Haimen, China). DyLight 488 goat anti-rabbit IgG and DyLight 594 goat anti-rabbit were purchased from Proteintech Company (Wuhan, China).

2.2. Emulsion confined assembly of lecithin and Co-Q10

Lecithin and Co-Q10 were dissolved in 1 mL of $CHCl_3$ solution with a respective concentration of 10.0 g L^{-1} and 0.2 g L^{-1}2 mL of deionized water was then added and an oil-in-water (O/W) emulsion was formed after vortex mixing (1000 rpm) for 1 min. After that, the emulsion was stirred at 60 °C for 30 min to evaporate the internal organic phase. Then 2 ml of ethanol was added, the supernatant was removed by centrifugation, and the resulting assemblies were dispersed in deionized water for morphological characterization.

2.3. Sample preparation for morphological characterization

The samples were stained with uranyl acetate as the dye solution. First, one drop of ~5 μL of sample was cast onto the carbon-supported membrane copper mesh, and the excess sample was blotted off with filter paper after 2 min. Then one drop of ~5 μL of 1.5% uranyl acetate ethanol solution was dropped, and the excess solution was blotted off with filter paper after 30 s. Finally, the copper mesh loaded with the

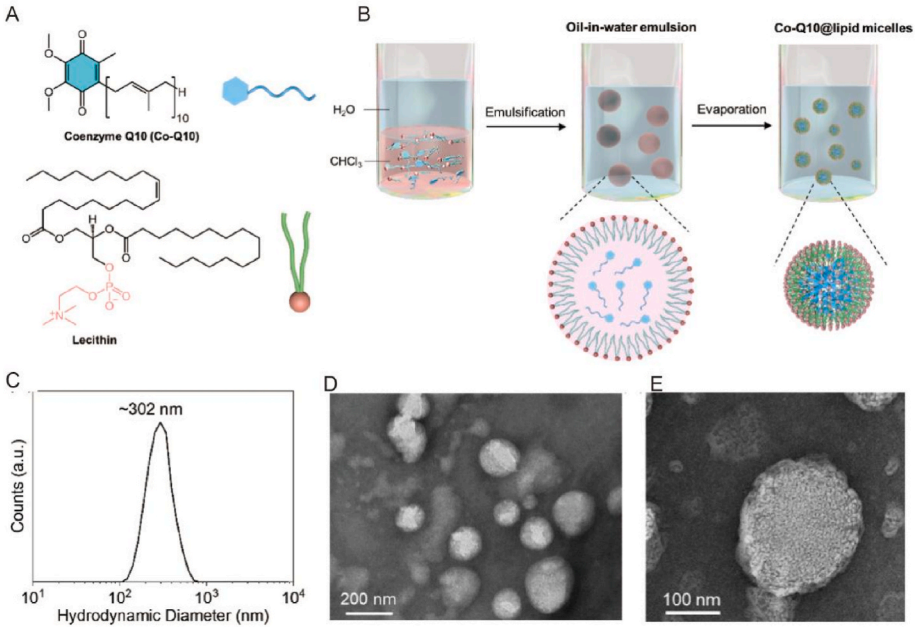

Fig. 1. Preparation and characterization of the LM@Co-Q10. (A) Molecular structure of lipid and Co-Q10. (B) Scheme for the preparation procedure. (C) DLS plot of the LM@Co-Q10. (D–E) TEM images of the LM@Co-Q10 negatively stained by uranyl acetate. (Scale bar = 200 nm, 100 nm).

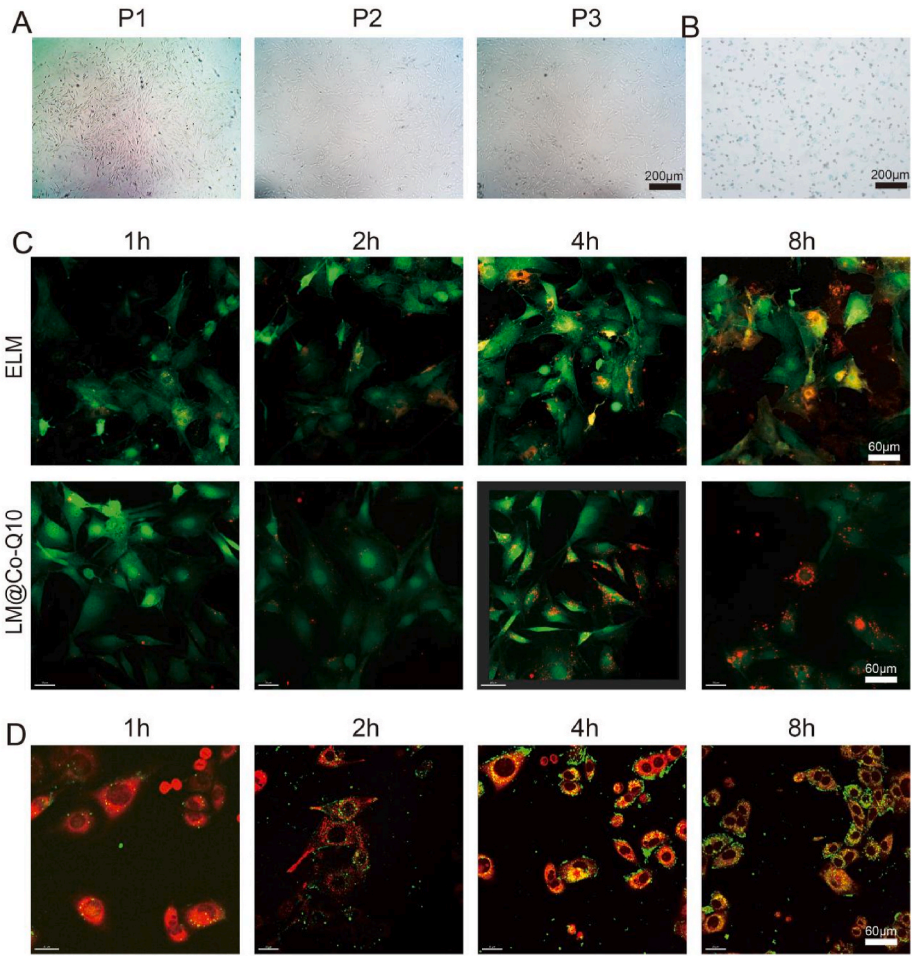

Fig. 2. Morphology of BMSCs and intracellular uptake and distribution of lipid micelles. (A) The morphology of BMSCs with different algebra. (Scale bar = 200 μm). (B) The β-Galactosidase stain of BMSCs. (Scale bar = 200 μm) (C) Intracellular uptake of ELM and LM@Co-Q10. The ELM and LM@Co-Q10 labeled with DiI appeared red dots, and the cells transfected with GFP lentivirus were green. (Scale bar = 60 μm) (D) The colocalization of LM@Co-Q10 and mitochondrion. The LM@Co-Q10 labeled with DiO appeared green dots, and mitochondria stained red by Mitotraker. (Scale bar = 60 μm).

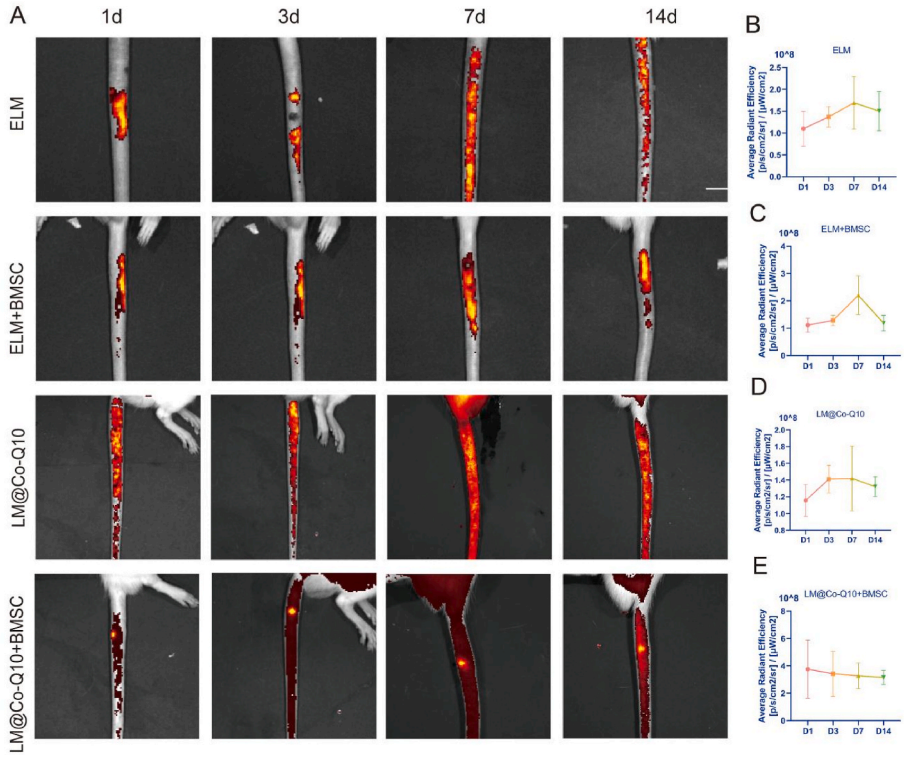

Fig. 3. *In vivo* distribution of lipid micelles. (A) Biodistribution of Different groups. The intervertebral fluorescence signal of rats was shown by IVIS. (B–E) The fluorescence signal intensity for different groups at different time.

sample was placed in a desiccator overnight.

2.4. Structural characterizations

The size of the emulsion droplets was measured using a laser particle size and zeta potential analyzer (Malvern). Transmission electron microscopy (TEM) characterization was performed on a Hitachi HT7700 microscope operating at 100 kV.

2.5. Isolation and characterization of mesenchymal stem cells from rat bone marrow

Isolation of bone mesenchymal stem cells (BMSCs) was carried out as previously depicted [28] with some changes. Four-week-old male Sprague-Dawley rats (Beijing Vital River Laboratory Animal Technology Co., Ltd.) were sacrificed and their femurs and tibiae were put in 75% alcohol by volume for sterilization. The ends of the tibia and femur were cut by scissors. A 27-gauge needle were inserted and flushed with Dulbecco's Modified Eagle's Medium/Nutrient Mixture F-12 (DMEM/F12). The cell suspension was filtered through a 70-μm filter mesh. The cells were cultured in DMEM/F12 + 10% FBS+1% antibiotic-antimycotic solution and incubated at 37 °C with 5% CO2. The medium was replaced for the first time after 24 h and was replaced every 3 days afterward. Passage 3–5 (P3–P5) cells were used for subsequent experiments.

For phenotype characterization, BMSCs were incubated with rabbit anti-rat polyclonal antibodies CD29, CD31, CD90, and CD45 (Biolegend, USA) and analyzed by flow cytometry (Beckman Cytoflex™, USA). In addition, to determine the multipotential differentiation capabilities of rat BMSCs, including osteogenic and adipogenic differentiation, BMSCs were cultured in the following medium types: (1) HyCyte™ F344 Rat Bone Marrow Mesenchymal Stem Cell Osteogenic Differentiation Medium. (2) HyCyte™F344 Rat Bone Marrow Mesenchymal Stem Cell Adipogenic Differentiation Medium. The induction medium was changed every 3 days. At day 14, cells were fixed and stained with Alizarin Red S for osteo-cytes, and Oil Red O for adipocytes (Cas9X™, China).

2.6. Senescence-associated β-galactosidase staining

β-Galactosidase staining was done with a senescence-associated β-Galactosidase Staining Kit (Beyotime, China). BMSCs were washed three times with PBS and fixed for 15 min at room temperature. Next, the cells were incubated overnight at 37 °C in darkness with the working solution containing 0.05 mg/ml 5-bromo-4-chloro-3-indolyl-β-D-galactopyranoside (X-gal)). The cells were observed with a bright-field microscope (Axio Vert.A1, Zeiss, Germany).

2.7. Intracellular uptake of LM@Co-Q10

DiI was utilized as a fluorescence probe to investigate the cellular uptake ability of ELM and LM@Co-Q10, with BMSCs transfected by GFP lentivirus. The solution was ultracentrifuged to remove free DiI after a small amount of DiI added. BMSCs separately cultured in culture plates (5×10^4 cells/well) were incubated with the culture medium containing DiI-labeled ELM and LM@Co-Q10 for 1, 2, 4 and 8 h. Confocal microscope (Andor, UK) was used to observe the fluorescence.

To visualize the colocalization of LM@Co-Q10 and mitochondrion, DiO was utilized as a fluorescence probe. BMSCs separately cultured in culture plates (5×10^4 cells/well) were incubated with the culture medium containing DiO-labeled LM@Co-Q10 for 1, 2, 4 and 8 h. The cells were washed and stained with Mitotracker (Ex/Em: 579/599 nm) for 30 min. Confocal microscope (Andor, UK) was used to observe the fluorescence.

2.8. Biodistribution and retention of LM@Co-Q10 in vivo

DiI-labeled ELM, DiI-labeled ELM and BMSCs, DiI-labeled LM@Co-Q10, DiI-labeled LM@Co-Q10 and BMSCs dissolved in PBS (2 μL) separately were injected into rats' intervertebral space. All rats were

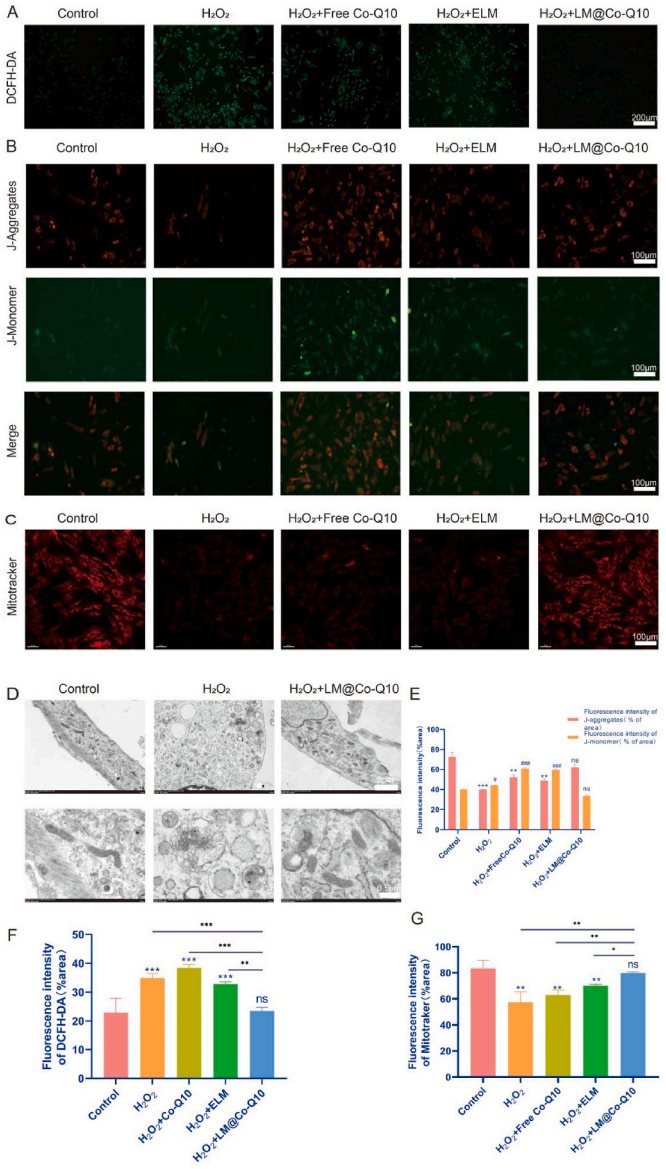

Fig. 4. LM@Co-Q10 suppressed H_2O_2-induced mitochondrial ROS and oxidative stress in BMSCs. (A) Intracellular ROS detection by DCFH-DA. (Scale bar = 200 μm) (B) Mitochondrial membrane potential of BMSCs assessed through JC-1 assay. JC-1 monomer was stained green, and JC-1 aggregates was stained red. (Scale bar = 100 μm) (C) Mitochondrial function of BMSCs evaluated by Mitotracker. (Scale bar = 100 μm) (D) TEM images of BMSCs in control group, H_2O_2 group and H_2O_2+LM@Co-Q10 group. (Scale bar = 2 μm and 500 nm) (E) Relative quantification of JC-1 fluorescence. (F) Quantification of relative ROS level. (G) Relative quantification of Mitotracker fluorescence. The data discussed above were presented as mean ± SD. ns (no statistical significance), $*p < 0.05$, $**p < 0.01$ and $***p < 0.001$ vs the control group; ns (no statistical significance), $\#p < 0.05$, $\#\#p < 0.01$ and $\#\#\#p < 0.001$ vs the LM@Co-Q10 group. n = 3.

placed in a darkroom (IVIS Spectrum, PerkinElmer, USA) to detect DiI fluorescence (Ex/Em: 549/565 nm) at different time points (1, 3, 7 and 14 d). At day 14, the rats were sacrificed to harvest adjacent vertebrae and major organs for ex vivo imaging.

2.9. Cell treatments and groups

The BMSCs were randomly divided into 5 groups: Control group (incubated with normal medium), H_2O_2 group (incubated with medium containing H_2O_2), H_2O_2+Free Co-Q10 group (incubated with medium containing H_2O_2 and Free Co-Q10), H_2O_2+ ELM group (incubated with medium containing H_2O_2 and ELM), and H_2O_2+LM@Co-Q10 group (incubated with medium containing H_2O_2 and LM@Co-Q10).

2.10. Intracellular ROS detection

The BMSCs were cultured in 24-well plates (2×10^4/well) and then treated with different groups. After 24 h, the BMSCs were incubated with dichloro-dihydro-fluorescein diacetate (DCFH-DA) (Beyotime, China) at 37 °C for 30 min. Then the BMSCs were washed three times with PBS. The ROS level was measured by fluorescence microscope (Zeiss, Germany).

2.11. Mitochondria-protection of LM@Co-Q10

The BMSCs were incubated in 24-well plates (2×10^4/well) overnight. Then the cells were exposed to various treatments for 24 h. The cells were washed and stained with Mitotracker (Ex/Em: 579/599 nm) for 30 min. Then, the cells were washed and observed by confocal microscopy. Besides, the mitochondrial membrane potential detection kit (JC-1) was also applied to determine the protective effect of LM@Co-Q10 in mitochondria. In brief, the BMSCs were stained with JC-1 solution for 30 min. The BMSCs were observed by confocal microscope (Andor, UK).

2.12. Cell viability evaluation

BMSCs in the exponential growth phase were seeded in 96-well plates at a density of 2×10^3 cells/well. After the treatments, the BMSCs were incubated for 24 h. CCK-8 kit (Sigma-Aldrich, USA) was used to test the cytotoxicity. A microplate reader was used to measure the absorbance of each well at 450 nm. The live/dead assay kit (Beyotime, China) was used to conduct live/dead assays. The images were taken using confocal fluorescence microscope (Andor, UK).

2.13. qRT-PCR assessment

Total mRNA was extracted from BMSCs using RNA fast 200 (Fastagen, Shanghai). Purified RNA was reverse transcribed into cDNA using qPCR-RT Master Mix (Toyobo, Japan). Finally, a real-time quantitative analysis of genes was performed with SYBR Green Realtime PCR Master Mix (Toyobo, Japan). Relative mRNA expression levels were normalized to an internal control and calculated according to the 2-ΔΔCT method. GAPDH was used as the internal control.

2.14. Western blot assessment

RIPA lysis buffer including protease inhibitors (Sigma-Aldrich, USA) was used to lyse the BMSCs. Then, the solution was centrifuged at 12,000 rpm at 4 °C for 15 min. SDS-PAGE was used to separate proteins at 80 V. Then proteins were transferred onto 0.22 μm polyvinylidene fluoride membranes (Millipore, USA) at 260 mA. QuickBlock™ blocking buffer (Beyotime, China) was used to block the membranes at room temperature for 20 min. Then the membranes were treated with the following primary antibodies at 4 °C overnight: ACAN (1:1000, Abcam), COL2 (1:1000; Abcam), SOX9 (1:1000, Abcam), KRT19 (1:1000, Cell Signaling Technology), COX2 (1:1000, Abcam), MMP-13 (1:1000, Abcam), iNOS (1:1000, Proteintech), Adamts-5 (1:1000, Affnity), TNF-α (1:1000, Abcam), BAX (1:1000, Abcam), Bcl2 (1:1000, Abcam), Caspase-3 (1:1000, Cell Signaling Technology), P65 (1:1000, Cell Signaling Technology), NF-κB (1:1000, Cell Signaling Technology), IKB α (1:1000, Proteintech), β-Actin and GAPDH (1:1000, Santa Cruz). Finally, the membranes were incubated with secondary antibodies (1:2000, Proteintech) at room temperature for 1 h. An enhanced chemiluminescence kit (Millipore, USA) was applied to detect the membranes. Protein contents were quantified by Image J software.

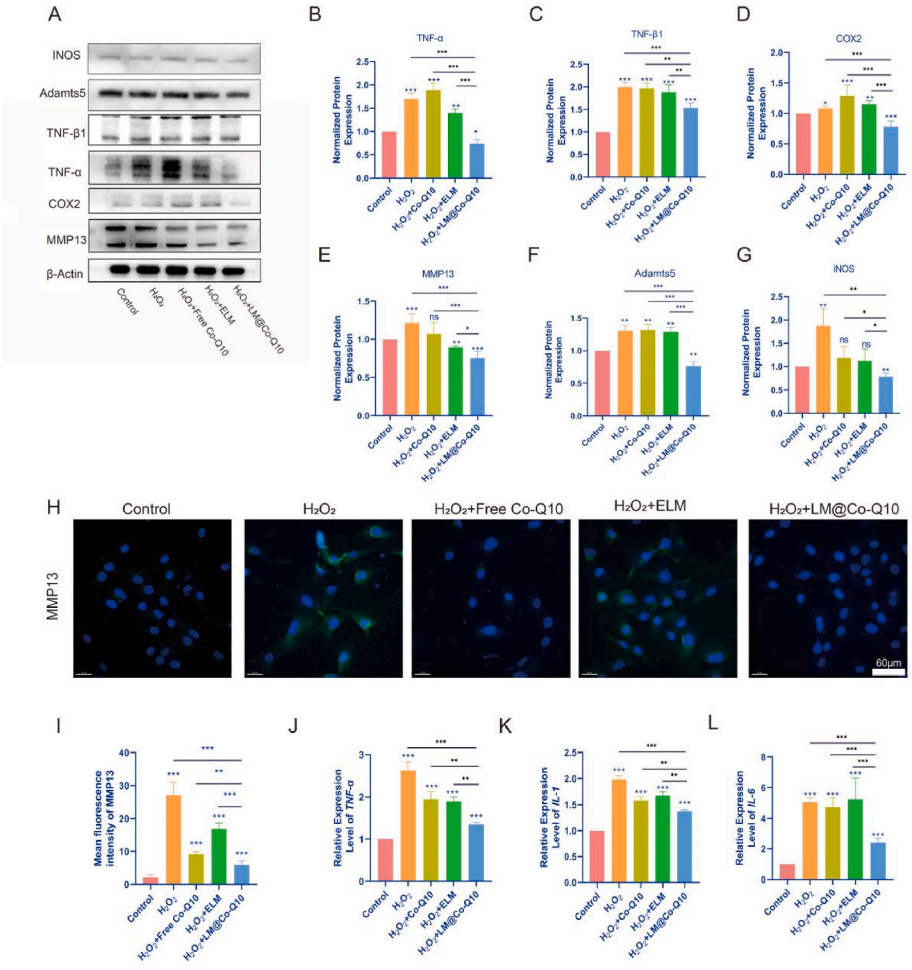

Fig. 5. Attenuation of H_2O_2-induced inflammatory responses and metabolic disorders in BMSCs by LM@Co-Q10. (A) Expression level of inflammatory response-related proteins on BMSCs with different treatments. (B–G) Quantification of inflammatory response-related proteins was calculated from A by Image J. (H) Immunofluorescence images of MMP13 (green) in different groups of BMSCs. (Scale bar = 60 μm) (I) Quantification of green areas from H using Image J. (J–L) The semi-quantitative analysis of IL-1, IL-6 and TNF-α mRNA expressions. The data were presented as mean ± SD. ns (no statistical significance), $*p < 0.05$, $**p < 0.01$ and $***p < 0.001$ vs the control group. n = 3.

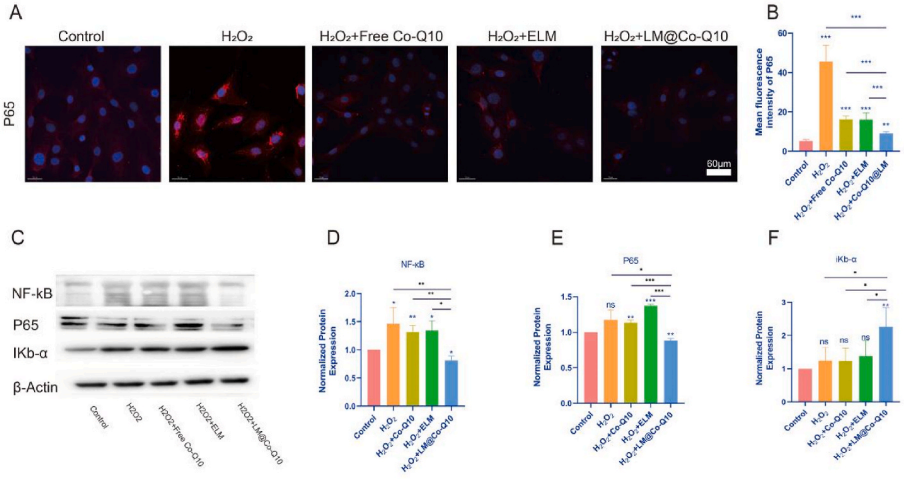

Fig. 6. LM@Co-Q10 antagonized the activation of the NF-κB signaling pathway. (A) Immunofluorescence images of P65 (red) in different groups of BMSCs. (Scale bar = 60 μm) (B) Quantification of red areas from A using Image J. (C) Expression level of NF-κB pathway-related proteins on BMSCs with different treatments. (D–F) Quantification of NF-κB pathway-related proteins was calculated from C by Image J. The data were presented as mean ± SD. ns (no statistical significance), $*p < 0.05$, $**p < 0.01$ and $***p < 0.001$ vs the control group. n = 3.

2.15. Immunofluorescence staining

BMSCs were cultured in 24-well plates at a density of 2×10^4 cells per well. After incubated with various treatments, the cells were fixed and incubated with the primary antibodies MMP13 (1:100), P65 (1:100), Col2 (1:100), SOX9 (1:100) overnight at 4 °C. Afterward, the cells were incubated with secondary antibodies for 1 h. After stained with DAPI for 5 min, the images were acquired using confocal microscope (Andor, UK). The mean fluorescence intensity was calculated based on Image J software.

2.16. RNA-seq analysis

Total RNA was extracted from the tissue using TRIzol® reagent according to the manufacturer's protocol (Invitrogen, USA) and genomic DNA was removed using DNase I (TaKara, Japan). Then RNA quality

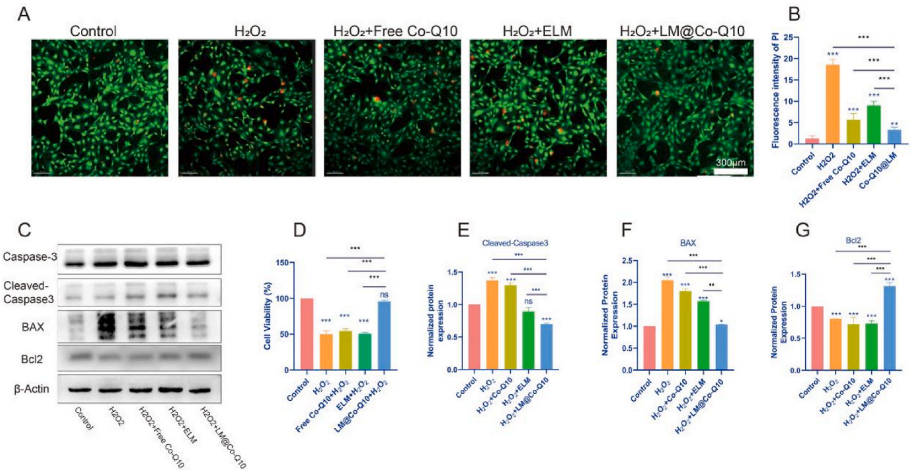

Fig. 7. LM@Co-Q10 reduced H_2O_2 induced-apoptosis of BMSCs. (A) Calcein-AM (green)/PI (red) staining of BMSCs after incubation with various treatments. (Scale bar = 300 μm) (B) Semiquantitative analysis of dead cells stained with PI (red) from A. (C) Expression level of apoptosis-related proteins on BMSCs with different treatments. (D) Cell viability of BMSCs after different treatments. (E–G) Quantification of apoptosis-related proteins was calculated from C by Image J. The data were presented as mean ± SD. ns (no statistical significance), $*p < 0.05$, $**p < 0.01$ and $***p < 0.001$ vs the control group. n = 3.

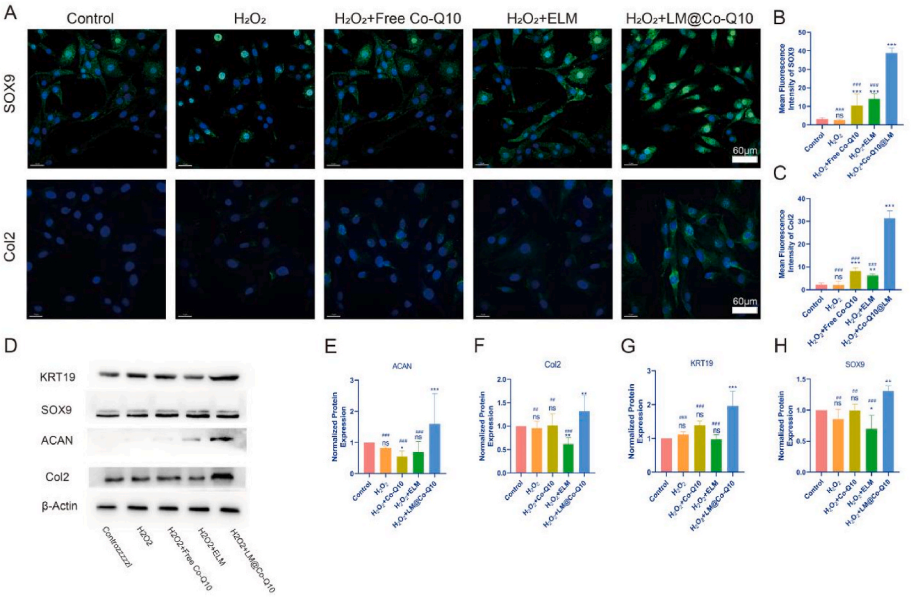

Fig. 8. The differentiation efficiency of BMSCs in the NP with LM@Co-Q10. (A) Representative fluorescence images of SOX9 (red) and Col2 (green) in the NPs under different treatments. (Scale bar = 40 μm, 60 μm) (B,C) Semiquantitative analysis of SOX9 and Col2 from A. (D) Expression level of differentiation-related proteins on BMSCs with different treatments. (E–H) Quantification of differentiation-related proteins was calculated from D by Image J. The data were presented as mean ± SD. ns (no statistical significance), $*p < 0.05$, $**p < 0.01$ and $***p < 0.001$ vs the control group; $\#p < 0.05$, $\#\#p < 0.01$ and $\#\#\#p < 0.001$ vs the LM@Co-Q10 group. n = 3.

was determined using 2100 Bioanalyser (Agilent, USA) and quantified using an ND-2000 spectrophotometer (NanoDrop Thermo Scientific, USA). Only high-quality RNA samples (OD260/280 = 1.8–2.2, OD260/230 ≥ 2.0, RIN≥6.5, 28S:18S ≥ 1.0, and >1 μg) were used to construct sequencing library. Sequencing was performed with the Illumina platform. The raw paired end reads were trimmed and quality controlled by FastQC (http://www.bioinformatics.bbsrc.ac.uk/projects/fastqc/) and Cutadapt (http://cutadapt.readthedocs.org/) with default parameters. Then clean reads were separately aligned to reference genome with orientation mode using HISAT2 (version:2.1.0) and SAMtools software (version: 1.3.1). The mapped reads from each sample were assembled by StringTie using a reference-based approach. A correlation heatmap and principal component analysis (PCA) were performed with DESeq2 based on the gene expression data. The expression level of each transcript was calculated using the transcripts per million reads (TPM) method to identify DEGs (differential expression genes) between two different samples. Significantly differentially expressed genes (DEGs) (logfold change ≥1, p-adjusted < 0.05) between BMSCs control group and LM@Co-Q10 were assessed using DESeq2. In addition, functional-enrichment analysis including Gene Ontology (GO) and Kyoto Encyclopedia of Genes and Genomes (KEGG) were performed to identify GO terms and metabolic pathways in which DEGs were significantly enriched in at a Bonferroni-corrected p value ≤ 0.05 compared with the whole-transcriptome background.

2.17. Animal surgery

Briefly, the SD rats were anesthetized with isoflurane. The intervertebral discs of caudal spine were identified by palpation. Then, we inserted a 17-gauge sterile needle with a manual stopper into the middle of the disc at a depth of 5 mm, rotated it 360°, and held it for 60 sec. 30 male rats with a mean weight of 270 g were randomly divided into 6 groups: The control group (without needle puncture); The puncture group (with needle puncture and PBS injection); The BMSCs group (with needle puncture and rat BMSCs injection); The Free Co-Q10 with rat BMSCs group (with needle puncture, free Co-Q10 and rat BMSCs injection). The ELM with rat BMSCs group (with needle puncture, ELM and rat BMSCs injection). The LM@Co-Q10 with rat BMSCs group (with needle puncture, LM@Co-Q10 and rat BMSCs injection). 2 μl of material was injected into the nucleus pulposus (NP) by a 31-gauge needle. The rats were executed after 4 weeks, independent IVDs of different groups were obtained for futher experiments.

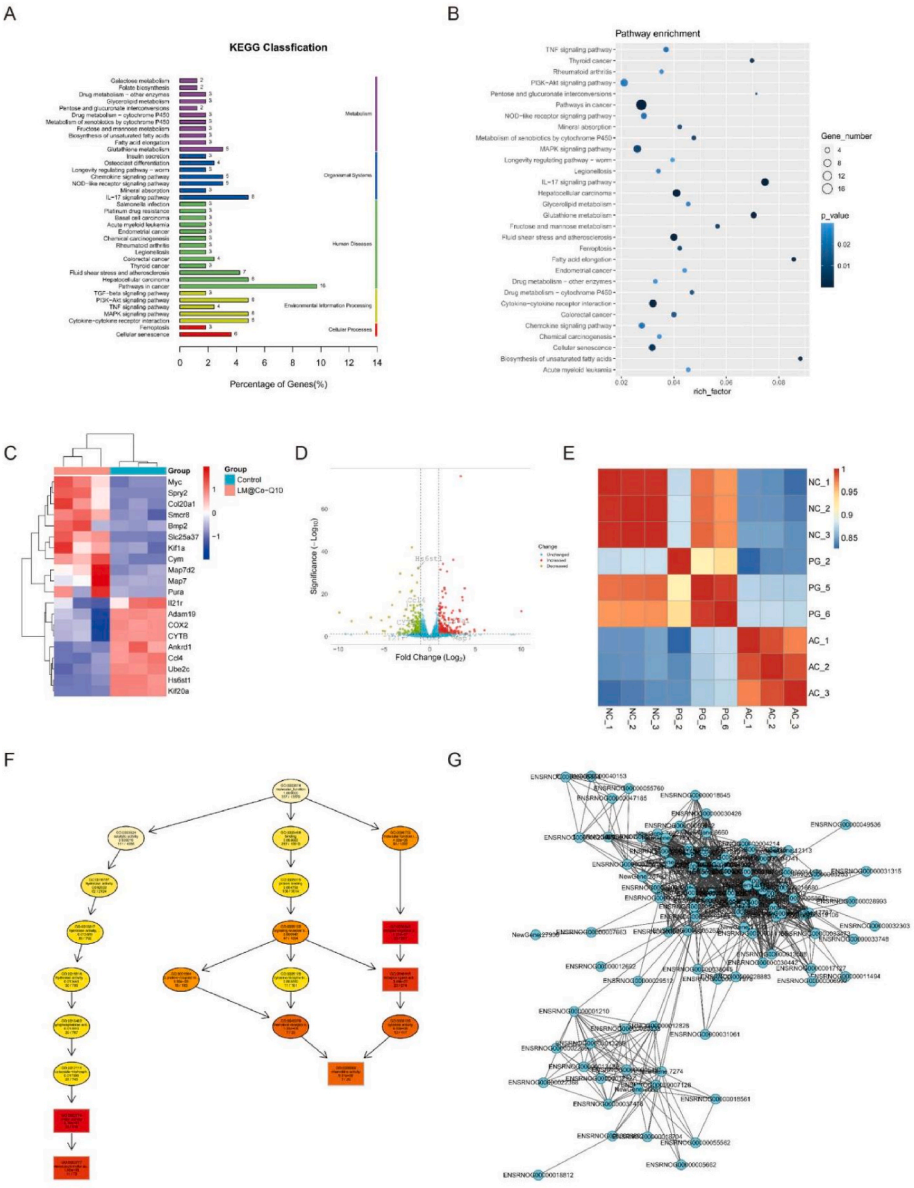

Fig. 9. Biobehavioral differences produced by LM@Co-Q10 treatment of BMSCs. (A) KEGG enrichment analysis of up-regulated pathways in BMSCs in the control and LM@Co-Q10 groups. (B) KEGG bubble plots of the pathways up-regulated in BMSCs in the control and LM@Co-Q10 groups. (C) Heat map of differentially expressed genes in BMSCs in the control group and LM@Co-Q10 group. (D) Volcano plot of differentially expressed genes in BMSCs in the control group and LM@Co-Q10 group. (E) Correlation heat map of gene expression of BMSCs in the control group, H_2O_2 group and LM@Co-Q10 group. (F) Results of GO enrichment analysis for the top 10 directed acyclic plots. (G) Different gene-gene interaction networks in the control group and LM@Co-Q10 groups. n = 3.

2.18. X-ray evaluation

X-ray (GE XR650, USA) was applied to assess disc height of the independent IVDs. Digital images were obtained using the radiographic plate system included with the instrument. The disc height index (DHI) was measured by Image J.

2.19. Magnetic resonance imaging (MRI) evaluation

A 3.0 T MRI scanner (GE Signa HDX, USA) was used to obtain the rat tail. The structure of NP was evaluated by T2-weighted sequence in the coronal plane. We placed the rats in the supine position and straightened their tails. The parameters of the MRI scanner were set as follows: spin echo repetition time, 2275 m s; echo time, 80 m s; number of excitations, 8; field of view, 5 cm; slice thickness, 1.5 mm; no phase wrap. MRI images were analyzed by Image J.

2.20. Histological evaluation

The intervertebral discs were fixed in 4% paraformaldehyde followed by paraffin embedding. Tissue sections were mounted on glass slides using a microtome (Leica, Germany). Hematoxylin-eosin (H&E) and safranin O-fast green (S–O) were performed according to standard protocols. Photographs were obtained with a panoramic digital slice scanning microscope (Olympus, Japan). Major organs were also acquired. H&E staining of major organs (heart, liver, spleen, lungs and kidneys) was also carried out.

2.21. TUNEL apoptosis assay

The sections were stained using the TUNEL apoptosis detection kit (Servicebio, China) according to the standard protocols, and apoptotic cells exhibited red fluorescence. The nuclei of the cells were stained with DAPI. Finally, the fluorescent images were taken by microscope. The quantitative results were presented as the percentage of TUNEL-positive cells relative to the total cells in the area.

2.22. Immunofluorescence staining in vivo

For immunofluorescence staining, sections were deparaffinized and hydrated as the protocol in immunohistochemical staining, endogenous peroxidase was blocked with 5% hydrogen peroxide for 15 min and

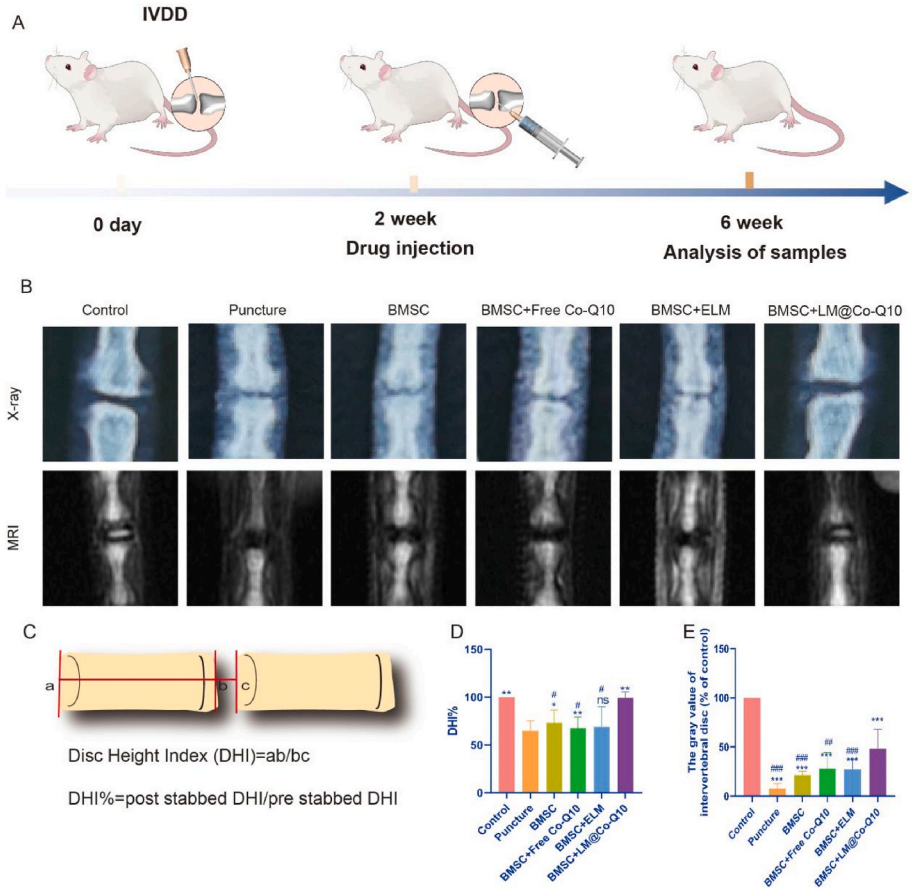

Fig. 10. Radiological evaluation *in vivo*. (A) Schematic illustration of the puncture-induced IVDD model and LM@Co-Q10 injection for the treatment. (B) X-ray and MRI images of the caudal vertebrae of rats at 4 weeks after different treatments. (C) The measurement schematic and formulas of disc height index. (D) Changes in disc height at 4 weeks after different treatments on X-ray. (E) Changes in discs at 4 weeks after different treatments on MRI. The data were presented as mean ± SD. ns (no statistical significance), $*p < 0.05$, $**p < 0.01$ and $***p < 0.001$ vs the puncture group; $\#p < 0.05$, $\#\#p < 0.01$ and $\#\#\#p < 0.001$ vs the BMSCs + LM@Co-Q10 group. n = 3.

nonspecific binding was blocked with 5% BSA for 30 min, respectively. Primaries were applied for NF-κB (1:200) and IKB-α (1:200) diluted in PBS overnight at 4 °C. The secondary antibodies were added followed by nuclear staining with DAPI for 5 min. Finally, the fluorescent images were taken by microscope.

2.23. Immunohistochemistry evaluation

For immunohistochemical evaluation, the sections were deparaffinized and incubated in 3% H_2O_2, then immersing in sodium citrate buffer at 95 °C. The slices were incubated with primary antibodies (anti-type II collagen (1:100), anti-MMP-13 (1:100), anti–NF–κB (1:100)) overnight at 4 °C, followed by incubating with secondary antibodies. After rinsing with PBST, the slices were incubated with DAB (3,3′-diaminobenzidine) kit (ZSGB-BIO, China) for visualization. Then the slices were washed in tap water, counterstained with hematoxylin, dehydrated, and coversliped with neutral resin. Images were taken by a panoramic digital slice scanning microscope (Olympus). Immunopositivity within the fields was calculated using Image-Pro Plus software.

2.24. Statistical analysis

The data were presented as mean ± SD. Statistical analysis was performed with the *t*-test and one-way ANOVA analysis (SPSS software, version 26.0, SPSS Inc). $p < 0.05$ was considered as statistically significant.

3. Results

3.1. Preparation and characterization of the Co-Q10@lipid micelles (LM@Co-Q10)

The LM@Co-Q10 was prepared through an emulsion based confined assembly method (Fig. 1A–B). After synthesis, these micelles could be well dispersed in water. Dynamic light scattering (DLS) measurement was carried out to determine the hydrodynamic diameter of these LM@Co-Q10, which is roughly 302 nm (Fig. 1C). TEM measurement was conducted to characterize the morphology and the size of the LM@Co-Q10. The sample was negatively stained with uranyl acetate, which was used to enhance the contrast of the TEM imaging. TEM images showed that spherical particles of ~200–300 nm in diameter were produced, which was consistent with the DLS measurement (Fig. 1D–E). We noted that these colloidal particles were quite stable under ambient conditions, which could be used for biological purposes.

3.2. Cell culture and co-localization of BMSCs and lipid micelles

To confirm that rBMSCs has the ability to proliferate, we obtained representative photomicrographs (Fig. 2A) and β-galactosidase stain (Fig. 2B) of rBMSCs. The cellular interaction behavior of ELM and LM@Co-Q10 was investigated using confocal microscopy. The ELM and LM@Co-Q10 was pre-labeled with DiI dye. The ELM and LM@Co-Q10 labeled with DiI appeared as red dots, while the cells transfected with GFP lentivirus were green. As shown in Fig. 2C, ELM and LM@Co-Q10 aggregated and accumulated to the BMSCs in a time-dependent manner. To visualize the colocalization of LM@Co-Q10 and mitochondrion, DiO was utilized as a fluorescence probe. As shown in Fig. 2D, The LM@Co-Q10 labeled with DiO appeared as green dots, while the

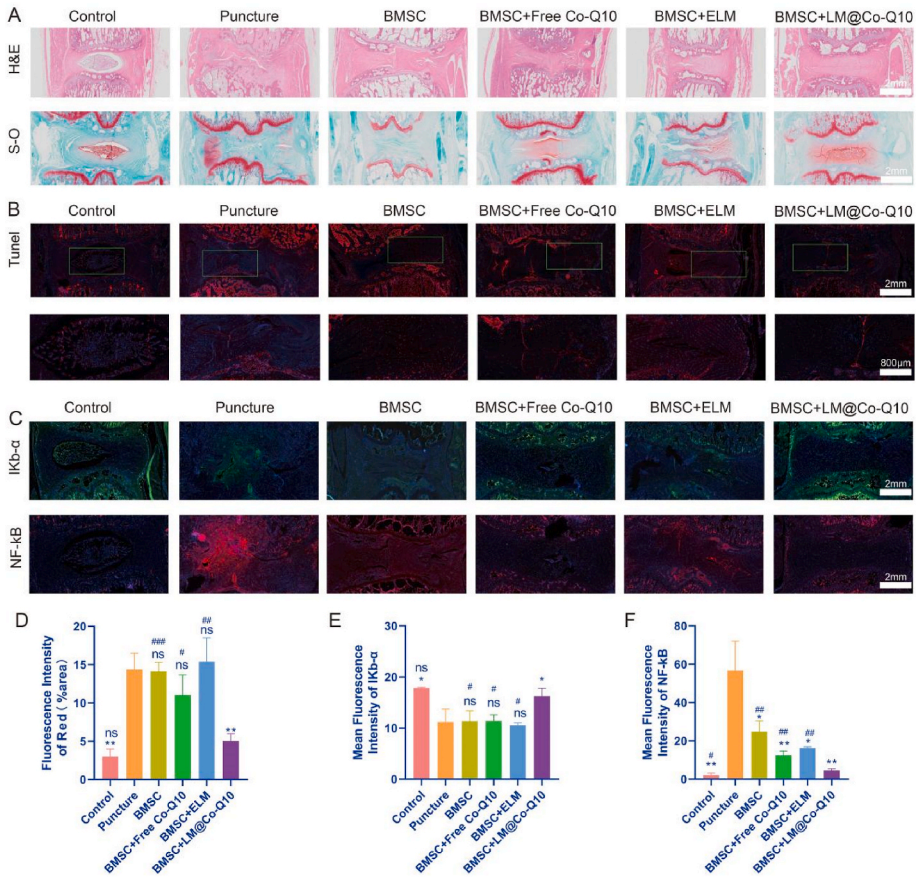

Fig. 11. Histological images *in vivo*. (A) H&E and Safranin O-fast green staining of NP in different groups. (Scale bar = 2 mm) (B) Tunel staining of NP in different groups (TUNEL positive: red). (Scale bar = 2 mm, 800 μm) (C) *In vivo* immunofluorescence images of NF-κB and IKB-α in the NP in different groups. (Scale bar = 2 mm) (D) Quantification of red areas from B. (E, F) Mean fluorescence intensity of NF-κB and IKB-α. The data were presented as mean ± SD. ns (no statistical significance), $*p < 0.05$, $**p < 0.01$ and $***p < 0.001$ vs the puncture group; ns (no statistical significance), $\#p < 0.05$, $\#\#p < 0.01$ and $\#\#\#p < 0.001$ vs the BMSCs + LM@Co-Q10 group. n = 3.

mitochondria stained red by Mitotracker. LM@Co-Q10 similarly accumulates in mitochondria in a time-dependent manner.

3.3. *In vivo* distribution of lipid micelles

The *in vivo* biodistribution of LM@Co-Q10 was further evaluated. After injecting ELM and LM@Co-Q10 which tagged by DiI into the intervertebral discs of SD rats, the fluorescence signals were detected at 1, 3, 7 and 14 days, respectively. There was obvious fluorescence signal in the intervertebral discs, which could still be observed even after 14 days (Fig. 3A).Meanwhile, except for LM@Co-Q10 + BMSC group, all the remaining groups had drug leakage from the intervertebral space, indicating that LM@Co-Q10 + BMSC group could produce the best therapeutic effect. The fluorescent signals of adjacent vertebrae and major organs were shown in Fig. S1. The signal intensity was much less than that of NP tissue *in vivo*, indicating that the LM@Co-Q10 did not accumulate in the aforementioned tissues.

3.4. Biodistribution and biosafety of LM@Co-Q10

To investigate the biological effects of LM@Co-Q10 *in vitro*, we cultured BMSCs with media containing different concentrations of LM@Co-Q10 to assess its possible cytotoxicity. The results showed that the number of cells did not decrease after 1, 7 and 14 days of incubation with different concentrations of LM@Co-Q10. In addition, H&E staining of the major organs showed no significant pathological changes in any group, indicating that LM@Co-Q10 had good biocompatibility *in vivo* (Fig. S2).

3.5. LM@Co-Q10 suppressed H_2O_2-induced mitochondrial ROS and oxidative stress in BMSCs

The antioxidant activity of LM@Co-Q10 was measured by the following methods. First, intracellular ROS level was assessed using DCFH-DA probe (Fig. 4A and F), demonstrating that H_2O_2 generally induced an increase in intracellular ROS in BMSCs, while the treatment with LM@Co-Q10 attenuated the ROS level. These results revealed that LM@Co-Q10 could promote BMSCs to resist oxidative stress. Moreover, the mitochondrial membrane potential of BMSCs was assessed through JC-1 assay, which indicated that H_2O_2 disturbed mitochondrial function, while additional treatment with LM@Co-Q10 almost reversed this trend under H_2O_2 stimulation (Fig. 4B and E). Furthermore, it was confirmed by Mitotracker staining that LM@Co-Q10 greatly improved the function of mitochondria in the presence of H_2O_2 (Fig. 4C and G). Finally, as observed by TEM, mitochondria was disrupted in the presence of H_2O_2, mainly in the form of mitochondrial fracture and swelling, and the administration of LM@Co-Q10 greatly attenuated this alteration (Fig. 4D).

3.6. Attenuation of H_2O_2-induced inflammatory responses and metabolic disorders in BMSCs by LM@Co-Q10

Exaggerated inflammatory microenvironment was commonly detected in the pathogenesis of IVDD. In this study, BMSCs were stimulated with H_2O_2 in the presence of PBS, ELM, Co-Q10 or LM@Co-Q10. Then, inflammatory biomarkers were detected by real-time PCR (Fig. 5J–L), western blot (Fig. 5A–G) and immunofluorescence (Fig. 5H and I). As a result, gene expression level and protein level of pro-inflammatory factors, including IL-1, IL-6, TNF-α, TNF-β1, COX2 and iNOS were enhanced by H_2O_2, while the inflammatory response was greatly alleviated with LM@Co-Q10. Disorders of metabolism was a

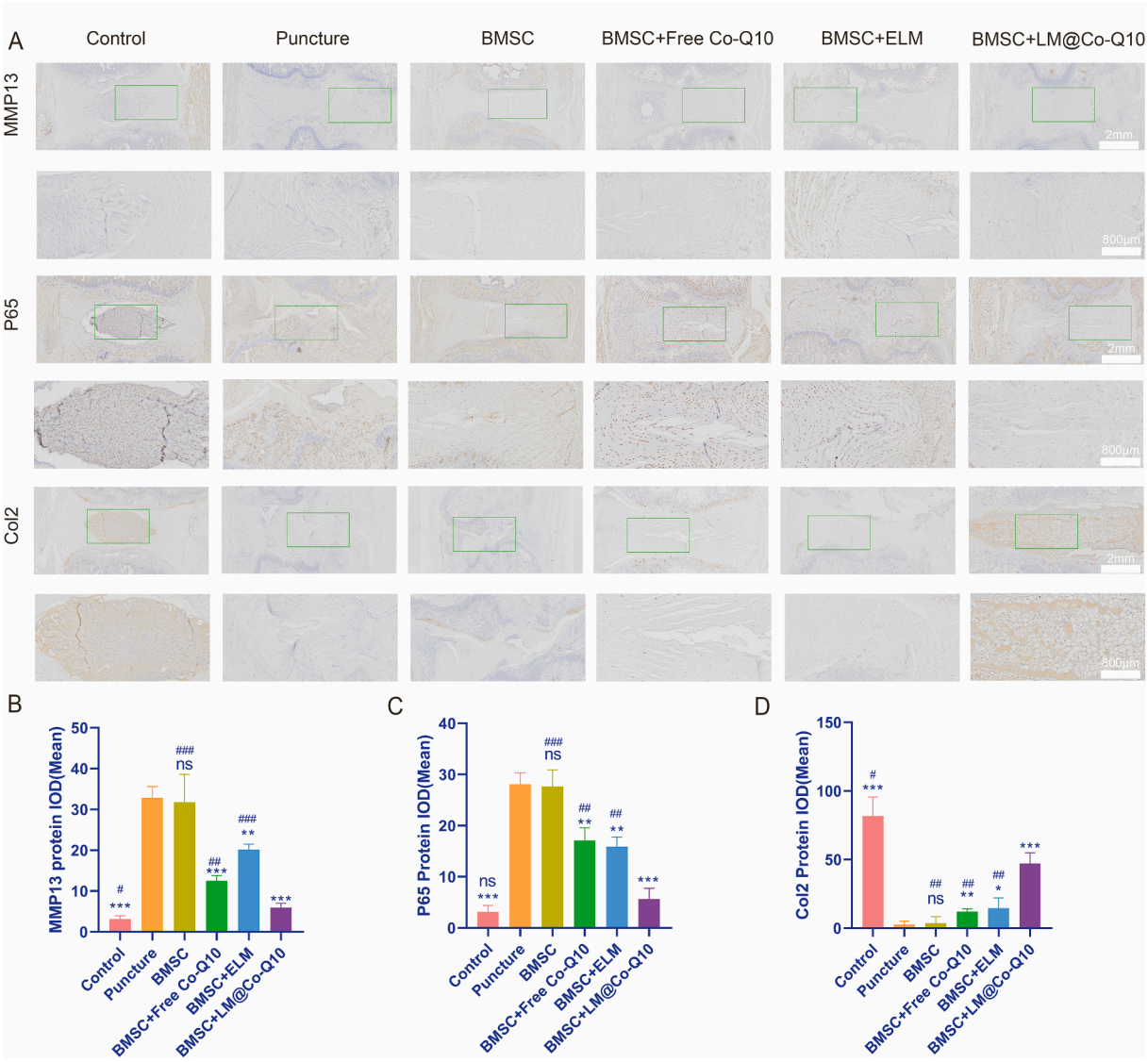

Fig. 12. Immunohistochemistry images *in vivo*. (A) IHC analysis of MMP13, P65 and Col2 in the NP in different groups (IHC positive: brown). (Scale bar = 2 mm, 800 μm) (B–D) Quantitative analysis of MMP13, P65 and Col2 in various treatments. The data were presented as mean ± SD. ns (no statistical significance), $*p < 0.05$, $**p < 0.01$ and $***p < 0.001$ vs the puncture group; ns (no statistical significance), $\#p < 0.05$, $\#\#p < 0.01$ and $\#\#\#p < 0.001$ vs the BMSCs + LM@Co-Q10 group. n = 3.

critical feature during the aging process. To date, catabolic factors, including MMP13, had been reported as the major factors in the metabolic disorders of cartilage structures. To demonstrate ECM degradation in IVDD, we used western blot (Fig. 5A and E) and immunofluorescence (Fig. 5H and I) to evaluate the expression of MMP13 in various treatments. As a result, H_2O_2 stimulation elevated the levels of the mentioned biomarkers, but this increase was greatly reduced by LM@Co-Q10. In short, LM@Co-Q10 showed the strongest ability to resist oxidative stress-induced ECM degradation. These results indicated that H_2O_2-induced inflammation and disorder of metabolism in BMSCs were dramatically suppressed by LM@Co-Q10.

3.7. LM@Co-Q10 antagonized the activation of the NF-κB signaling pathway

Activation of the NF-κB signaling pathway was well known to play an important role in the development of IVDD. After the above treatment of BMSCs, we extracted the total proteins of the cells for analysis to explore whether LM@Co-Q10 protected against IVDD by inhibiting the NF-κB signaling pathway. Notably, IKb-α and P65 were important indicators used to measure the activation of the NF-κB signaling pathway. As shown in Fig. 6C–E, relative to the H_2O_2 group, the protein level of NF-κB and P65 expression decreased after LM@Co-Q10 treatment. In Fig. 6F, the protein level of IκBα increased after treatment with LM@Co-Q10 compared with the H_2O_2 group. In addition, immunofluorescence of P65 showed that H_2O_2 elevated the expression of P65 as well as enhanced nuclear translocation, while LM@Co-Q10 decreased the expression of P65 and reduced nuclear translocation (Fig. 6A and B).

3.8. LM@Co-Q10 reduced H_2O_2 induced-apoptosis of BMSCs

The viability of rat BMSCs was assessed by cell counting kit-8 (CCK-8) assay and live/dead staining. As seen in Fig. 7A, B and 7D, the mortality rate of H_2O_2-induced BMSCs decreased dramatically after treatment with LM@Co-Q10. To verify the intrinsic mechanism of apoptosis, western blotting was used in this experiment. The expression of proteins such as BAX and Caspase 3 (17kD) decreased under LM@Co-Q10 treatment, while the expression of proteins such as Bcl2 increased under LM@Co-Q10 treatment (Fig. 7C, E, F and G).

3.9. The differentiation efficiency of BMSCs in the NP with LM@Co-Q10

The matrix-synthesis ability of BMSCs was determined by the gene expression and protein levels of ACAN and Col2, all of which were higher in the H_2O_2+LM@Co-Q10 group than the control, H_2O_2, H_2O_2+ELM, and H_2O_2+Co-Q10 groups on day 21 (Fig. 8D-F). Previous studies detected the positive correlation between the expression of the transcription factor SOX9 and the maintenance of healthy ECM [36]. The LM@Co-Q10 group also showed the highest expression level of SOX9 (Fig. 8D and H). KRT19 exhibited a high percentage of expression in the NP-like tissues, making it an ideal marker for NP cells [37]. In this study, BMSCs cultured with LM@Co-Q10 showed higher levels of KRT19 compared to the ELM or Co-Q10 groups (Fig. 8D and G). Immunofluorescence of Col2 and SOX9 indicated that LM@Co-Q10 greatly induced the differentiation of BMSCs to the NP-like phenotype (Fig. 8A-C). All these data demonstrated that LM@Co-Q10 displayed a strong potential to inhibit the degradation of ECM and to mediate the myeloid differentiation of BMSCs under oxidative stress.

3.10. Biobehavioral differences induced by LM@Co-Q10 treatment of BMSCs

Based on the distinct biological behaviours, we further compared differences in the transcriptome of control group, H_2O_2 group and LM@Co-Q10 group by RNA-seq analysis to explore the possible mechanisms. BMSCs were harvested after 14 days of *in vitro* culture for total RNA extraction, RNA-seq transcriptome library construction, DEG (differentially expressed gene) identification and functional enrichment analysis (GO and KEGG). The statistics of up-regulated and down-regulated genes in the LM@Co-Q10 group compared to the control group were shown in the heat map (Fig. 9C). Notably, according to the KEGG analysis, the up-regulated DEGs in the LM@Co-Q10 group were enriched in biological processes related to the regulation of collagen fibril organization, which may explain why the BMSCS in the LM@Co-Q10 group had more potential for functional ECM synthesis than the control group (Fig. 9A and B). Furthermore, KEGG enrichment analysis revealed that several pathways highly relevant to ECM metabolism and oxidative phosphorylation were activated in the LM@Co-Q10 group. Also, the interactions of differential genes in different treatment groups were represented by directed acyclic plots and gene - gene interaction networks, which also explained the above mentioned changes in gene expression levels (Fig. 9F and G).

3.11. LM@Co-Q10 improves therapeutic efficiency of transplanted BMSCs in rat coccygeal IVD D model

To further investigate the function of LM@Co-Q10 *in vivo*, rat coccygeal IVDD model was established, and 2×10^5 BMSCs treated with PBS, Co-Q10, ELM and LM@Co-Q10 were injected into the NP tissue (Fig. 10A). After 4 weeks, the height of the IVD was evaluated by X-ray to assess the treatment effect of LM@Co-Q10 *in vivo* (Fig. 10B). The disc height index (DHI%) values were significantly lower in the puncture group compared to the control group. The DHI% values were elevated in the BMSCs, BMSCs+Co-Q10, BMSCs+ELM and BMSCs+LM@Co-Q10 compared to the puncture group, with the highest DHI% values in the BMSCs + LM@Co-Q10 group ($p < 0.01$) (Fig. 10D). In addition, MRI was a valid assessment method to evaluate the water content and composition of IVD (Fig. 10B). Based on the signal assessment system [28], the BMSCs+LM@Co-Q10 group greatly attenuated the signal loss induced by IVD ($p < 0.001$) (Fig. 9E).

To investigate the therapeutic effect in more detail, immunohistochemistry and immunofluorescence were performed. According to HE staining, the control group showed intact disc structure. However, intervertebral disc structure in the puncture group was disrupted and showed reduced disc contents with disorganized hypocellular fibrocartilage tissue. Although the punctured discs in the BMSCs+LM@Co-Q10 group were still degraded to some extent, the BMSCs+LM@Co-Q10 group displayed more intact disc morphology than the BMSCs, BMSCs+Co-Q10 and BMSCs+ELM groups (Fig. 11A). Safranin-O staining demonstrated a decrease in proteoglycans in the puncture and BMSCs groups (Fig. 11A). The BMSCs+Co-Q10 and BMSCs+ELM groups showed evidence of partial damage repair, but the BMSCs+LM@Co-Q10 group showed marked improvement. In addition, intervertebral disc structure in the control group showed no marked cell apoptosis, while substantial apoptosis occurred in the puncture, BMSCs, BMSCs+Co-Q10, BMSCs+ELM groups (Fig. 11B and D). However, it was noteworthy that the apoptosis could be reversed in BMSCs+LM@Co-Q10 group.

NF-κB and IKB-α, played a pivotal role in NF-κB signaling pathway. As shown in Fig. 11C, NF-κB drastically reduced in BMSCs+LM@Co-Q10 group. In contrast, The expression of IKB-α after treatment with BMSCs+LM@Co-Q10 was higher than that of other post-puncture treatment groups.

The IHC images also suggested that the BMSCs+LM@Co-Q10 group suppressed the Col2 expression and enhanced the MMP13 and P65 expression in the punctured discs extensively (Fig. 12A). The data demonstrated that the combined treatment of BMSCs and LM@Co-Q10 had a stronger restorative effect for IVDD.

4. Discussion

In the current study, we proposed a potential strategy for enhancing BMSCs transplantation treatment efficiency in IVDD. Both *in vitro* (BMSCs) and *in vivo* (a rat IVDD model) were performed to validate mechanism as well as effectiveness of the proposed therapy. As the core of our strategy for IVDD treatment, we prepared water-dispersible Co-Q10-based assemblies, and their surfaces were coated with a layer of lipid molecules, rendering these colloidal assemblies amphiphilic. Our work demonstrates that LM@Co-Q10 could protect MSCs from oxidative stress, and enhance differentiation of MSCs into an NP-like phenotype.

As a promising strategy for IVDD treatment, stem cell transplantation therapy attracts much attention [29,30]. BMSCs are multipotent cells featured by their ability to differentiate into several cell types [31–33]. Previous studies have investigated the beneficial function of BMSCs on intervertebral disc degeneration [34–36]. Nevertheless, there are still tough problems to be elucidated between the microenvironment and transplanted cells. Although physical production of ROS serves as signaling molecule in cells, excessive oxidative and inflammation production is detrimental and has been commonly detected in development of IVDD [37,38]. ROS stimulation as well as nonspecific inflammation are leading cause of transplanted stem cells generated during the IVDD. Cellular damage and dysfunction are closely associated with high ROS levels [39,40]. Therefore, Attenuation of ROS-induced cell apoptosis and promotion of cell differentiation were essential for getting greater clinical success in cell transplantation therapy [41]. In the current study, LM@Co-Q10 largely abolished the detrimental role of H_2O_2 in oxidative stress of BMSCs and protected against production of ROS.

It is known that mitochondrial function plays a critical role in viability of stem cells. In this study, H_2O_2 administration imitated a harsh environment for transplantation of MSCs and led to mitochondrial dysfunction and enhanced apoptosis of BMSCs, which is in consistence with previous reports [42]. Nevertheless, LM@Co-Q10 exhibited great effect to protect against this alteration, suggesting the therapeutic efficiency of Co-Q10 is markedly enhanced through liquid micelle delivery pattern.

The anti-aging and anti-apoptotic capability of Co-Q10 has been reported on several conditions. Our present study confirmed that Co-Q10 stimulated the proliferation and survival rate of BMSCs on IVDD. Secondly, micelles established by lipid have been proved to be safe and efficient for local and systemic delivery of drugs, and this drug delivery strategy has been shown to enhance proliferation and cell differentiation of BMSCs [43]. Although previous studies have shown regenerative functions of stem cell transplantation in IVDD to a certain extent,

strategies are still required to fight against excessive oxidative stress in the local site, which leads to hyper-peroxidation, protein carbonylation as well as DNA damage to transplanted BMSCs. Intriguingly, we have herein determined that efficient delivery of antioxidant Co-Q10 through liquid micelles increases BMSCs viability through reducing inflammation factors (COX2, iNOS) and catabolic biomarkers (MMP-13, ADAMTS-5), suppressing ROS production. In addition, Co-Q10 released from our micelles attenuates apoptosis through protecting against mitochondrial dysfunction. NF-κB signaling pathway is closely associated with inflammation and aging process under oxidative stress, and results in upregulation of various genes which plays a detrimental role in IVDD. Previous studies demonstrated that Co-Q10 represses exaggerated activation of NF-κB signaling pathway to enhance the intracellular antioxidant properties of BMSCs. There might thus exist a potential relationship between LM@Co-Q10 and oxidative stress induced NF-κB signaling pathway to suppress ROS and disorder of inflammation as well as metabolism [44]. The relationship discussed above may explain the anti-oxidative ability of LM@Co-Q10. Furthermore, histological assessments confirm that LM@Co-Q10 delivery effectively elevated the protective function of transplanted BMSCs in IVDD progression and nucleus pulposus degradation, and this is the main finding of our study to facilitate BMSCs to fight against oxidative stress.

KRT19 is a specifically expressed biomarker in NP-like cells. Moreover, Col2 and Aggrecan are commonly tested as anabolic factors in evaluating the extracellular matrix releasing ability of differentiated cells [45]. Totally, the differentiation and extracellular matrix production ability of BMSCs can be effectively assessed using these genes in this study. Strikingly, the levels of mentioned biomarkers in BMSCs were greatly retained following treatment of LM@Co-Q10 in stimulation of H_2O_2, suggesting the efficiency of micelle delivery strategy in facilitating Co-Q10 into BMSCs, which consequently fight against oxidative stress.

Our previous studies described a coccygeal disc degeneration model generated via needle puncture. This animal model facilitates injection of micelles into the injury area, and histologic as well as radiographic signs of degeneration in IVD can be consequently monitored [46]. IVDD is featured by loss of disc height, ECM, water content and NP cell number [47]. Our results show that injection of LM@Co-Q10 with BMSCs yields better results than in the degeneration, ELM and Co-Q10 groups. In the degeneration group, IVD structures were obviously destroyed. In our study, the morphology of the NP was evaluated by histological score. The histological score of the LM@Co-Q10 group was significantly lower than that of either ELM, Co-Q10 or the degeneration group. Although IVDD was indeed attenuated in the Co-Q10 group, its histological score was still higher than that in LM@Co-Q10 group. Furthermore, injection of ELM has no obvious activity on alleviating IVDD. This result may be due to the intracellular delivery efficiency of Co-Q10 on BMSCs, which leads to reduction of ROS and apoptotic cell, and maintenance of the differentiation and proliferation potential of BMSCs.

5. Conclusions

In our study, an injectable Co-Q10-loaded micelle, LM@Co-Q10 was developed to efficiently deliver Co-Q10 into BMSCs for treatment of IVDD. The results demonstrate the biosafety of LM@Co-Q10, and its ability to mediate differentiation of BMSCs and to protect cells by antagonizing oxidative stress. As a result, LM@Co-Q10 combined with BMSCs could attenuate IVDD *in vivo*, providing a potential strategy in developing biological therapies for IVDD.

Ethics approval

The animal study was reviewed and approved by the Research Ethics Committee of Shandong University Qilu Hospital.

CRediT authorship contribution statement

Xuesong Zhang, Xinyu Liu, Yunpeng Zhao and **Junyuan Sun** designed the experiments. **Junyuan Sun** conducted most of the experiments. **Fei Yang** and **Zhijie Yang** helped with the synthesis of Co-Q10-loaded micelle. **Lianlei Wang** helped with animal experiments. **Haichao Yu** helped with the histological evaluation. **Jingjing Wei** and **Krasimir Vasilev** helped with the statistical analysis. **Junyuan Sun** and **Fei Yang** outlined and wrote the paper.

Junyuan Sun, Fei Yang, Lianlei Wang, Haichao Yu contributed equally to this work, and should be considered as equal first author. Xuesong Zhang, Xinyu Liu, Yunpeng Zhao contributed equally to this work, and should be considered as equal corresponding author.

Declaration of competing interest

The authors declare no competing financial interest.

Acknowledgements

This work was supported by National Natural Science Foundation of China (Grant No. 82072478 to Yunpeng Zhao), Shandong Provincial Natural Science Foundation (Grant No. ZR2020YQ54, ZR019MH05 to Yunpeng Zhao); National Natural Science Foundation of China (Grant No. 81874022, 82172483 to Xinyu Liu); National Natural Science Foundation of China (Grant No. 81972128to Xuesong Zhang) and Application of Clinical Features of Capital City of Science and Technology Commission China BEIJING Special subject (Z181100001718180 to Xuesong Zhang); National Nature Science Foundation (82102522 to Lianlei Wang), Shandong Natural Science Foundation (ZR202102210113 to Lianlei Wang) and Shandong Province Taishan Scholar Project.

Appendix A. Supplementary data

Supplementary data to this article can be found online at https://doi.org/10.1016/j.bioactmat.2022.10.019.

References

[1] GBD 2017 Disease and Injury Incidence and Prevalence Collaborators, Global, regional, and national incidence, prevalence, and years lived with disability for 354 diseases and injuries for 195 countries and territories, 1990-2017: a systematic analysis for the Global Burden of Disease Study 2017, Lancet (London, England) 392 (10159) (2018) 1789–1858, https://doi.org/10.1016/S0140-6736(18)32279-7.

[2] J.M. Stevans, A. Delitto, S.S. Khoja, C.G. Patterson, C.N. Smith, M.J. Schneider, J. K. Freburger, C.M. Greco, J.A. Freel, G.A. Sowa, A.D. Wasan, G.P. Brennan, S. J. Hunter, K.I. Minick, S.T. Wegener, P.L. Ephraim, M. Friedman, J.M. Beneciuk, S. Z. George, R.B. Saper, Risk factors associated with transition from acute to chronic low back pain in US patients seeking primary care, JAMA Netw. Open 4 (2) (2021), e2037371, https://doi.org/10.1001/jamanetworkopen.2020.37371.

[3] B. Sun, M. Lian, Y. Han, X. Mo, W. Jiang, Z. Qiao, K. Dai, A 3D-Bioprinted dual growth factor-releasing intervertebral disc scaffold induces nucleus pulposus and annulus fibrosus reconstruction, Bioact. Mater. 6 (1) (2020) 179–190, https://doi.org/10.1016/j.bioactmat.2020.06.022.

[4] J. Li, C. Marmorat, G. Vasilyev, J. Jiang, N. Koifman, Y. Guo, I. Talmon, E. Zussman, D. Gersappe, R. Davis, M. Rafailovich, Flow induced stability of pluronic hydrogels: injectable and unencapsulated nucleus pulposus replacement, Acta Biomater. 96 (2019) 295–302, https://doi.org/10.1016/j.actbio.2019.07.021.

[5] M. Nadeau, S.D. McLachlin, S.I. Bailey, K.R. Gurr, C.E. Dunning, C.S. Bailey, A biomechanical assessment of soft-tissue damage in the cervical spine following a unilateral facet injury, J. Bone Jt. Surg. Am. Vol. 94 (21) (2012), e156, https://doi.org/10.2106/JBJS.K.00694.

[6] X. Cheng, L. Zhang, K. Zhang, G. Zhang, Y. Hu, X. Sun, C. Zhao, H. Li, Y.M. Li, J. Zhao, Circular RNA VMA21 protects against intervertebral disc degeneration through targeting miR-200c and X linked inhibitor-of-apoptosis protein, Ann. Rheum. Dis. 77 (5) (2018) 770–779, https://doi.org/10.1136/annrheumdis-2017-212056.

[7] J. Zhang, Z. Li, F. Chen, H. Liu, H. Wang, X. Li, X. Liu, J. Wang, Z. Zheng, TGF-β1 suppresses CCL3/4 expression through the ERK signaling pathway and inhibits intervertebral disc degeneration and inflammation-related pain in a rat model, Exp. Mol. Med. 49 (9) (2017), e379, https://doi.org/10.1038/emm.2017.136.

[8] K. Sun, X. Jing, J. Guo, X. Yao, F. Guo, Mitophagy in degenerative joint diseases, Autophagy 17 (9) (2021) 2082–2092, https://doi.org/10.1080/15548627.2020.1822097.

[9] C. Yu, D. Li, C. Wang, K. Xia, J. Wang, X. Zhou, L. Ying, J. Shu, X. Huang, H. Xu, B. Han, Q. Chen, F. Li, J. Tang, C. Liang, N. Slater, Injectable kartogenin and apocynin loaded micelle enhances the alleviation of intervertebral disc degeneration by adipose-derived stem cell, Bioact. Mater. 6 (10) (2021) 3568–3579, https://doi.org/10.1016/j.bioactmat.2021.03.018.

[10] J. Tu, W. Li, S. Yang, P. Yang, Q. Yan, S. Wang, K. Lai, X. Bai, C. Wu, W. Ding, J. Cooper-White, A. Diwan, C. Yang, H. Yang, J. Zou, Single-cell transcriptome profiling reveals multicellular ecosystem of nucleus pulposus during degeneration progression, Adv. Sci. 9 (3) (2022), e2103631, https://doi.org/10.1002/advs.202103631.

[11] X. Zhou, J. Wang, X. Huang, W. Fang, Y. Tao, T. Zhao, C. Liang, J. Hua, Q. Chen, F. Li, Injectable decellularized nucleus pulposus-based cell delivery system for differentiation of adipose-derived stem cells and nucleus pulposus regeneration, Acta Biomater. 81 (2018) 115–128, https://doi.org/10.1016/j.actbio.2018.09.044.

[12] R. He, Z. Wang, M. Cui, S. Liu, W. Wu, M. Chen, Y. Wu, Y. Qu, H. Lin, S. Chen, B. Wang, Z. Shao, HIF1A Alleviates compression-induced apoptosis of nucleus pulposus derived stem cells via upregulating autophagy, Autophagy 17 (11) (2021) 3338–3360, https://doi.org/10.1080/15548627.2021.1872227.

[13] D. Sakai, G.B. Andersson, Stem cell therapy for intervertebral disc regeneration: obstacles and solutions, Nat. Rev. Rheumatol. 11 (4) (2015) 243–256, https://doi.org/10.1038/nrrheum.2015.13.

[14] J. Bai, Y. Zhang, Q. Fan, J. Xu, H. Shan, X. Gao, Q. Ma, L. Sheng, X. Zheng, W. Cheng, D. Li, M. Zhang, Y. Hao, L. Feng, Q. Chen, X. Zhou, C. Wang, Reactive oxygen species-scavenging scaffold with rapamycin for treatment of intervertebral disk degeneration, Advanced healthcare materials 9 (3) (2020), e1901186, https://doi.org/10.1002/adhm.201901186.

[15] W. Zhang, G. Li, R. Luo, J. Lei, Y. Song, B. Wang, L. Ma, Z. Liao, W. Ke, H. Liu, W. Hua, K. Zhao, X. Feng, X. Wu, Y. Zhang, K. Wang, C. Yang, Cytosolic escape of mitochondrial DNA triggers cGAS-STING-NLRP3 axis-dependent nucleus pulposus cell pyroptosis, Exp. Mol. Med. 54 (2) (2022) 129–142, https://doi.org/10.1038/s12276-022-00729-9.

[16] J. Oh, Y.D. Lee, A.J. Wagers, Stem cell aging: mechanisms, regulators and therapeutic opportunities, Nat. Med. 20 (8) (2014) 870–880, https://doi.org/10.1038/nm.3651.

[17] Y. Wang, S. Hekimi, Understanding ubiquinone, Trends Cell Biol. 26 (5) (2016) 367–378, https://doi.org/10.1016/j.tcb.2015.12.007.

[18] J. Cao, X. Liu, Y. Yang, B. Wei, Q. Li, G. Mao, Y. He, Y. Li, L. Zheng, Q. Zhang, J. Li, L. Wang, C. Qi, Decylubiquinone suppresses breast cancer growth and metastasis by inhibiting angiogenesis via the ROS/p53/Bai1 signaling pathway, Angiogenesis 23 (3) (2020) 325–338, https://doi.org/10.1007/s10456-020-09707-z.

[19] L.A. Kiyuna, R. Albuquerque, C.H. Chen, D. Mochly-Rosen, J. Ferreira, Targeting mitochondrial dysfunction and oxidative stress in heart failure: challenges and opportunities, Free Radic. Biol. Med. 129 (2018) 155–168, https://doi.org/10.1016/j.freeradbiomed.2018.09.019.

[20] N.M. Zaki, Strategies for oral delivery and mitochondrial targeting of CoQ10, Drug Deliv. 23 (6) (2016) 1868–1881, https://doi.org/10.3109/10717544.2014.993747.

[21] F. Emma, G. Montini, S.M. Parikh, L. Salviati, Mitochondrial dysfunction in inherited renal disease and acute kidney injury, Nat. Rev. Nephrol. 12 (5) (2016) 267–280, https://doi.org/10.1038/nrneph.2015.214.

[22] M. Zhang, X. ShiYang, Y. Zhang, Y. Miao, Y. Chen, Z. Cui, B. Xiong, Coenzyme Q10 ameliorates the quality of postovulatory aged oocytes by suppressing DNA damage and apoptosis, Free Radic. Biol. Med. 143 (2019) 84–94, https://doi.org/10.1016/j.freeradbiomed.2019.08.002.

[23] A. Ben-Meir, E. Burstein, A. Borrego-Alvarez, J. Chong, E. Wong, T. Yavorska, T. Naranian, M. Chi, Y. Wang, Y. Bentov, J. Alexis, J. Meriano, H.K. Sung, D. L. Gasser, K.H. Moley, S. Hekimi, R.F. Casper, A. Jurisicova, Coenzyme Q10 restores oocyte mitochondrial function and fertility during reproductive aging, Aging Cell 14 (5) (2015) 887–895, https://doi.org/10.1111/acel.12368.

[24] N. Omidifar, M. Moghadami, S.M. Mousavi, S.A. Hashemi, A. Gholami, M. Shokripour, Z. Sohrabi, Trends in natural nutrients for oxidative stress and cell senescence, Oxid. Med. Cell. Longev. 2021 (2021), 7501424, https://doi.org/10.1155/2021/7501424.

[25] F.M. Gutierrez-Mariscal, E.M. Yubero-Serrano, J.M. Villalba, J. Lopez-Miranda, Coenzyme Q10: from bench to clinic in aging diseases, a translational review, Crit. Rev. Food Sci. Nutr. 59 (14) (2019) 2240–2257, https://doi.org/10.1080/10408398.2018.1442316.

[26] I. Rabinovich-Nikitin, M. Rasouli, C.J. Reitz, I. Posen, V. Margulets, R. Dhingra, T. N. Khatua, J.A. Thliveris, T.A. Martino, L.A. Kirshenbaum, Mitochondrial autophagy and cell survival is regulated by the circadian Clock gene in cardiac myocytes during ischemic stress, Autophagy 17 (11) (2021) 3794–3812, https://doi.org/10.1080/15548627.2021.1938913.

[27] F.M. Gutierrez-Mariscal, A.P. Arenas-de Larriva, L. Limia-Perez, J.L. Romero-Cabrera, E.M. Yubero-Serrano, J. López-Miranda, Coenzyme Q10 supplementation for the reduction of oxidative stress: clinical implications in the treatment of chronic diseases, Int. J. Mol. Sci. 21 (21) (2020) 7870, https://doi.org/10.3390/ijms21217870.

[28] Y. Liu, L. Wang, R. Fatahi, M. Kronenberg, I. Kalajzic, D. Rowe, Y. Li, P. Maye, Isolation of murine bone marrow derived mesenchymal stem cells using Twist2 Cre transgenic mice, Bone 47 (5) (2010) 916–925, https://doi.org/10.1016/j.bone.2010.07.022.

[29] Y. Zeng, C. Chen, W. Liu, Q. Fu, Z. Han, Y. Li, S. Feng, X. Li, C. Qi, J. Wu, D. Wang, C. Corbett, B.P. Chan, D. Ruan, Y. Du, Injectable microcryogels reinforced alginate encapsulation of mesenchymal stromal cells for leak-proof delivery and alleviation of canine disc degeneration, Biomaterials 59 (2015) 53–65, https://doi.org/10.1016/j.biomaterials.2015.04.029.

[30] B. Bhujel, H.E. Shin, D.J. Choi, I. Han, Mesenchymal stem cell-derived exosomes and intervertebral disc regeneration: review, Int. J. Mol. Sci. 23 (13) (2022) 7306, https://doi.org/10.3390/ijms23137306.

[31] Y. Wang, X. Chen, W. Cao, Y. Shi, Plasticity of mesenchymal stem cells in immunomodulation: pathological and therapeutic implications, Nat. Immunol. 15 (11) (2014) 1009–1016, https://doi.org/10.1038/ni.3002.

[32] A. Rauch, S. Mandrup, Transcriptional networks controlling stromal cell differentiation, Nat. Rev. Mol. Cell Biol. 22 (7) (2021) 465–482, https://doi.org/10.1038/s41580-021-00357-7.

[33] C. Vater, P. Kasten, M. Stiehler, Culture media for the differentiation of mesenchymal stromal cells, Acta Biomater. 7 (2) (2011) 463–477, https://doi.org/10.1016/j.actbio.2010.07.037.

[34] Z. Liao, S. Li, S. Lu, H. Liu, G. Li, L. Ma, R. Luo, W. Ke, B. Wang, Q. Xiang, Y. Song, X. Feng, Y. Zhang, X. Wu, W. Hua, C. Yang, Metformin facilitates mesenchymal stem cell-derived extracellular nanovesicles release and optimizes therapeutic efficacy in intervertebral disc degeneration, Biomaterials 274 (2021), 120850, https://doi.org/10.1016/j.biomaterials.2021.120850.

[35] K. Lu, H.Y. Li, K. Yang, J.L. Wu, X.W. Cai, Y. Zhou, C.Q. Li, Exosomes as potential alternatives to stem cell therapy for intervertebral disc degeneration: in-vitro study on exosomes in interaction of nucleus pulposus cells and bone marrow mesenchymal stem cells, Stem Cell Res. Ther. 8 (1) (2017) 108, https://doi.org/10.1186/s13287-017-0563-9.

[36] H. Zhang, S. Yu, X. Zhao, Z. Mao, C. Gao, Stromal cell-derived factor-1α-encapsulated albumin/heparin nanoparticles for induced stem cell migration and intervertebral disc regeneration *in vivo*, Acta Biomater. 72 (2018) 217–227, https://doi.org/10.1016/j.actbio.2018.03.032.

[37] S. Yang, F. Zhang, J. Ma, W. Ding, Intervertebral disc ageing and degeneration: the antiapoptotic effect of oestrogen, Ageing Res. Rev. 57 (2020), 100978, https://doi.org/10.1016/j.arr.2019.100978.

[38] Z. Li, K. Zhang, X. Li, H. Pan, S. Li, F. Chen, J. Zhang, Z. Zheng, J. Wang, H. Liu, Wnt5a suppresses inflammation-driven intervertebral disc degeneration via a TNF-α/NF-κB-Wnt5a negative-feedback loop, Osteoarthritis Cartilage 26 (7) (2018) 966–977, https://doi.org/10.1016/j.joca.2018.04.002.

[39] K. Boengler, M. Kosiol, M. Mayr, R. Schulz, S. Rohrbach, Mitochondria and ageing: role in heart, skeletal muscle and adipose tissue, Journal of cachexia, sarcopenia and muscle 8 (3) (2017) 349–369, https://doi.org/10.1002/jcsm.12178.

[40] J.A. Fafián-Labora, J.A. Rodríguez-Navarro, A. O'Loghlen, Small extracellular vesicles have GST activity and ameliorate senescence-related tissue damage, Cell Metabol. 32 (1) (2020) 71–86, https://doi.org/10.1016/j.cmet.2020.06.004, e5.

[41] Z. Shi, D. Diao, Y. Zhao, Y. Luo, Y. Li, D. Liu, K. Zhang, Y. Qiu, L. Yu, Z. Song, Z. Ju, C/EBP homologous protein deficiency enhances hematopoietic stem cell function via reducing ATF3/ROS-induced cell apoptosis, Aging Cell 20 (7) (2021), e13382, https://doi.org/10.1111/acel.13382.

[42] G. Choe, S.W. Kim, J. Park, J. Park, S. Kim, Y.S. Kim, Y. Ahn, D.W. Jung, D. R. Williams, J.Y. Lee, Anti-oxidant activity reinforced reduced graphene oxide/alginate microgels: mesenchymal stem cell encapsulation and regeneration of infarcted hearts, Biomaterials 225 (2019), 119513, https://doi.org/10.1016/j.biomaterials.2019.119513.

[43] M.D. Cordero, E. Alcocer-Gómez, O. Culic, A.M. Carrión, M. de Miguel, E. Díaz-Parrado, E.M. Pérez-Villegas, P. Bullón, M. Battino, J.A. Sánchez-Alcazar, NLRP3 inflammasome is activated in fibromyalgia: the effect of coenzyme Q10, Antioxidants Redox Signal. 20 (8) (2014) 1169–1180, https://doi.org/10.1089/ars.2013.5198.

[44] E. Dayar, M. Cebova, J. Lietava, E. Panghyova, O. Pechanova, Antioxidant effect of Lonicera caerulea L. In the cardiovascular system of obese zucker rats, Antioxidants 10 (8) (2021) 1199, https://doi.org/10.3390/antiox10081199.

[45] B.O. Diekman, N. Christoforou, V.P. Willard, H. Sun, J. Sanchez-Adams, K. W. Leong, F. Guilak, Cartilage tissue engineering using differentiated and purified induced pluripotent stem cells, Proc. Natl. Acad. Sci. U. S. A. 109 (47) (2012) 19172–19177, https://doi.org/10.1073/pnas.1210422109.

[46] Y. Zhao, C. Qiu, W. Wang, J. Peng, X. Cheng, Y. Shangguan, M. Xu, J. Li, R. Qu, X. Chen, S. Jia, D. Luo, L. Liu, P. Li, F. Guo, K. Vasilev, L. Liu, J. Hayball, S. Dong, X. Pan, W. Li, Cortistatin protects against intervertebral disc degeneration through targeting mitochondrial ROS-dependent NLRP3 inflammasome activation, Theranostics 10 (15) (2020) 7015–7033, https://doi.org/10.7150/thno.45359.

[47] X. Cheng, J. Lin, Z. Chen, Y. Mao, X. Wu, C. Xu, J. Du, Z. Dong, H. Yang, F. Zhou, D. Geng, CB2-mediated attenuation of nucleus pulposus degeneration via the amelioration of inflammation and oxidative stress *in vivo* and *in vitro*, Mol. Med. (Camb.) 27 (1) (2021) 92, https://doi.org/10.1186/s10020-021-00351-x.